

See discussions, stats, and author profiles for this publication at: <https://www.researchgate.net/publication/231644291>

Synthesis and Luminescence Properties of Erbium-Doped Y₂O₃ Nanotubes

ARTICLE in THE JOURNAL OF PHYSICAL CHEMISTRY C · JANUARY 2008

Impact Factor: 4.77 · DOI: 10.1021/jp0773738

CITATIONS

85

READS

50

5 AUTHORS, INCLUDING:



Yuanbing Mao

University of Texas - Pan American

54 PUBLICATIONS 2,082 CITATIONS

SEE PROFILE



Kang L Wang

University of California, Los Angeles

968 PUBLICATIONS 17,514 CITATIONS

SEE PROFILE

Synthesis and Luminescence Properties of Erbium-Doped Y_2O_3 NanotubesYuanbing Mao,[†] Jian Y. Huang,[‡] Roman Ostroumov,[§] Kang L. Wang,[§] and Jane P. Chang^{*,†}

Department of Chemical and Biomolecular Engineering, University of California, Los Angeles, California 90095, Center for Integrated Nanotechnologies (CINT), Sandia National Laboratories, Albuquerque, New Mexico 87185, and Department of Electrical Engineering, University of California, Los Angeles, California 90095

Received: September 13, 2007; In Final Form: November 11, 2007

Erbium-doped yttrium oxide nanotubes ($\text{Er}^{3+}:\text{Y}_2\text{O}_3$ NTs) with 0–100% doping levels were synthesized by a hydrothermal procedure followed by a dehydration process from $\text{Er}^{3+}:\text{Y}(\text{OH})_3$ NTs. The as-synthesized $\text{Er}^{3+}:\text{Y}_2\text{O}_3$ nanotubes ranged from 100 to 400 nm in outer diameter and 2 to 5 μm in length with a hexagonal cross section. A time-dependent nanostructure evolution study was performed under hydrothermal conditions, and the effects of other processing parameters, including pH, concentration, and ionic strength of the precursor solution as well as the time span for adding the alkaline solution, were found to dictate the purity and morphology of the as-synthesized $\text{Er}^{3+}:\text{Y}(\text{OH})_3$ nanostructures. A kinetics-controlled dissolution–recrystallization mechanism is proposed to explain the anisotropic growth of these hollow nanotubes from the hexagonal crystal structure of yttrium and erbium hydroxides. Outstanding room-temperature photoluminescence around 1535 nm was demonstrated for these $\text{Er}^{3+}:\text{Y}_2\text{O}_3$ NTs, making them promising for optical amplifier, laser, and active waveguide applications in telecommunications.

Introduction

Novel light-emitting materials have received much attention for a few decades for their versatile applications in fiber-optic amplifiers, lasers, waveguides, X-ray imaging, bioimaging, field emission, and electroluminescent displays.^{1,2} Among them, inorganic luminescent materials have practical applications in almost any device involving the artificial production of light, such as well-known examples of cathode ray tubes, lamps, X-ray detectors, plasma displays, and field emission displays.^{1–9} Considerable research activity is being carried out to explore new luminescent materials, to improve their chemical stability, and to adapt their materials chemistry to the production technology for each application. In particular, rare earth ions (e.g., Er^{3+} and Eu^{3+}) incorporated in high refractive index media allow the development of tricolor lamps, field emission displays, lasers, and amplifiers.^{1,2,5} The emission of light from the rare earth ions is mainly due to electric and magnetic dipole optical transitions with the $4f^n$ energy manifolds and may also involve $4f^n-15d$. In general, the absorption and emission spectra of rare earth ions appear as sharp and narrow bands, whose positions are weakly dependent on the coordination environment or the crystal field.¹⁰

Trivalent erbium ion (Er^{3+}) is one of the species which has attracted most interest among luminescent rare-earth ions in recent years, mainly because its emission band is around 1535 nm, a wavelength of great interest for telecommunications.^{11,12} Since this wavelength corresponds to the minimum band loss of silica optical fibers, the Er-doped silica fiber amplifier (EDFA) is now a standard device for long-distance optical

telecommunication. A major challenge in EDFA is to incorporate a high concentration of optically active erbium ions in the silica host to achieve a reasonable gain value. In this regard, silicon dioxide is not a suitable host material due to its low solubility for erbium ions. With many recent research activities on studying new types of fibers and dopants, it is critical to evaluate new host materials.^{5,13} Specifically, yttrium oxide (Y_2O_3) is a promising host material for Er^{3+} because Er_2O_3 and Y_2O_3 have the same crystal structures with very similar lattice constants, and Y^{3+} and Er^{3+} trivalent ions have nearly the same ionic radii.^{10,14} In principle, Y_2O_3 would allow the incorporation of a much higher erbium concentration, compared to that in silicon dioxide. At the same time, Y_2O_3 has a broad transparency range (0.2–8 μm), a high melting point, a high refractive index, a low phonon energy, and excellent thermal conductivity and stability.^{8,10,14–17} All of these make Y_2O_3 a very attractive host material for erbium-doped optical waveguides and amplifiers. The majority of the previous work has focused on the Er-doped Y_2O_3 ($\text{Er}^{3+}:\text{Y}_2\text{O}_3$) single crystals and thin films.^{7,8,13,15,16,18–27} In fact, we synthesized $\text{Er}^{3+}:\text{Y}_2\text{O}_3$ thin films by radical-enhanced atomic layer deposition at 350 °C and demonstrated that the Er^{3+} incorporated in Y_2O_3 (6–14 at. %) can reach a concentration as high as 10^{21} cm^{-3} with spatially controlled distribution, along with promising room-temperature photoluminescence (PL) around 1535 nm.^{13,18}

Recently, nanostructures (e.g., nanoparticles, nanowires, and nanotubes) made of rare-earth ion-doped oxides have been investigated as emerging materials because they exhibit interesting physical properties, in particular, various emission lifetimes and increased luminescence efficiencies, which are different from those of their bulk counterparts.^{10,13,24,43–48} Therefore, they possess diverse potential applications in nanoscale electronics, photonics, and advanced bioanalysis.^{28,49} Rare-earth-doped Y_2O_3 nanomaterials have been synthesized by a variety of techniques such as the solution-based sol–gel process, gel combustion

* To whom correspondence should be addressed.

[†] Department of Chemical and Biomolecular Engineering, University of California at Los Angeles.

[‡] Center for Integrated Nanotechnologies (CINT), Sandia National Laboratories.

[§] Department of Electrical Engineering, University of California at Los Angeles.

synthesis, emulsion technique, coprecipitation method, hydrothermal method, template method, electrochemical method, or their combinations.^{14,21,22,31–35,39–44,46,50–52} There are more reports in recent years on one-dimensional (1-D) rare-earth ion-doped oxide nanostructures, an important building block for future optical and optoelectronic nanodevices.^{28,29} These 1-D $\text{Er}^{3+}:\text{Y}_2\text{O}_3$ nanostructures were primarily synthesized by template-directed procedures, using either carbon nanotubes or porous anodic alumina as templates, by hydrothermal routes followed by an annealing process, or by electrochemical processes.^{30–42}

In this study, we have extended these investigations to a series of $\text{Er}^{3+}:\text{Y}_2\text{O}_3$ nanotubes (NTs), which were prepared by a hydrothermal process followed by a dehydration reaction. The hydrothermal process is used because it is a well-established, closed-system and low-temperature method that is suited for large scale synthesis and can lead to energy savings. Furthermore, hydrothermal process usually provides highly crystallized products.^{53,54} Most importantly, it allows us to readily make Y_2O_3 NTs with various Er^{3+} doping levels.

Experimental Section

A. Sample Preparation. The $\text{Er}^{3+}:\text{Y}_2\text{O}_3$ NTs were prepared by a hydrothermal technique followed by a dehydration process, which is similar to previously reported procedure.^{33–36} Specifically, high-purity $\text{Y}(\text{NO}_3)_3$ and $\text{Er}(\text{NO}_3)_3$ (totally 1.5 mmol, with specifically adjusted $\text{Y}^{3+}/\text{Er}^{3+}$ molar ratios) were dissolved in 4 mL of deionized H_2O , followed by the dropwise addition of 14 mL of NaOH solution under stirring. After being stirred for 1 h, the milky colloid solution was transferred into a 23 mL Teflon-lined autoclave and subsequently sealed and heated at an appropriate temperature (e.g., 100, 130, or 180 °C) for 7 h. The resulting reaction solution along with the precipitate was cooled to room temperature naturally and then centrifuged. The colorless supernatant including reaction byproducts was discarded. The precipitate was washed with deionized water several times and then dried at 80 °C in air overnight. Finally, the obtained powder of $\text{Er}^{3+}:\text{Y}(\text{OH})_3$ NTs was placed into a ceramic crucible and converted into the corresponding powder of $\text{Er}^{3+}:\text{Y}_2\text{O}_3$ NTs by annealing at 500 °C for 3 h in a box furnace.

B. Measurements. *X-ray diffraction (XRD).* Powder XRD and synchrotron XRD were used to obtain the crystallographic and purity information on $\text{Er}^{3+}:\text{Y}(\text{OH})_3$ and $\text{Er}^{3+}:\text{Y}_2\text{O}_3$ NTs. To analyze the samples by powder XRD, the as-prepared samples of $\text{Er}^{3+}:\text{Y}(\text{OH})_3$ and $\text{Er}^{3+}:\text{Y}_2\text{O}_3$ NTs, after centrifugation, were subsequently sonicated for about 1 min and later air-dried upon deposition onto glass slides. Diffraction patterns of these materials were collected using a PANalytical X-ray diffractometer, operating in the Bragg configuration using $\text{Cu K}\alpha$ radiation ($\lambda = 1.54 \text{ \AA}$) from 10 to 80° at a scanning rate of 0.2°/min. For synchrotron XRD study, data were collected at the Stanford Synchrotron Radiation Laboratory on beamline 2-1 using an X-ray energy of 14 keV from 1.9 to 6.3 \AA^{-1} . The powder samples were pressed into the shallow cavity of a quartz sample holder. The loaded samples were rocked throughout the experiment in the X-ray beam to average the diffraction patterns.

Electron Microscopy. The size and morphology of solid powder samples of $\text{Er}^{3+}:\text{Y}(\text{OH})_3$ and $\text{Er}^{3+}:\text{Y}_2\text{O}_3$ NTs were characterized using a field emission scanning electron microscope (SEM, Hitachi S4700) at an accelerating voltage of 10 kV. Specifically, the as-prepared samples of $\text{Er}^{3+}:\text{Y}(\text{OH})_3$ and $\text{Er}^{3+}:\text{Y}_2\text{O}_3$ NTs, after centrifugation, were sonicated for about 1 min and later air-dried upon deposition onto clean silicon wafers, which were then attached onto the surfaces of SEM brass stubs. Low-magnification transmission electron microscopy

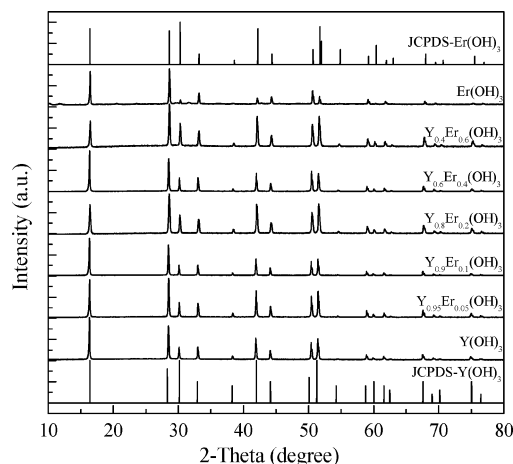


Figure 1. XRD patterns ($\text{Cu K}\alpha$) of $\text{Er}^{3+}:\text{Y}(\text{OH})_3$ NTs with various doping levels synthesized under hydrothermal conditions at 130 °C for 7 h.

(TEM) images were taken at an accelerating voltage of 120 kV on a JEOL JEM-100 CX instrument. High-resolution TEM (HRTEM) images, selected-area electron diffraction (SAED) patterns, energy-dispersive X-ray spectroscopy (EDS) data, and high-angle annular dark field (HAADF) images were carried out on an FEI Tecnai F30 transmission electron microscope equipped with an EDAX EDS detector and a HAADF detector. The microscope was operated at an accelerating voltage of 300 kV with a field emission source with a point-to-point resolution of 0.2 nm. HRTEM images were recorded by means of a Gatan CCD camera ($4k \times 4k$). The EDS experiments for thickness profile of isolated NTs were performed in the scanning TEM (STEM) mode using the HAADF detector with a camera length of 150 mm. The electron probe of 1 nm in diameter was scanned over an isolated NT surface with EDS spectra taken at each point. Experimental conditions were chosen such that the collection semiangle was 30 mrad. The EDS spectra were recorded using an EDS Si/Li detector with an ultrathin window. Specimens for the TEM studies were prepared by depositing a drop of the aqueous suspension of $\text{Er}^{3+}:\text{Y}(\text{OH})_3$ or $\text{Er}^{3+}:\text{Y}_2\text{O}_3$ NTs onto a 300 mesh Cu grid, coated with a lacey carbon film. Prior to the deposition, the solution containing $\text{Er}^{3+}:\text{Y}(\text{OH})_3$ or $\text{Er}^{3+}:\text{Y}_2\text{O}_3$ NTs was sonicated for 2 min to ensure adequate dispersion in solution.

Photoluminescence (PL). To characterize the optical properties of the $\text{Er}^{3+}:\text{Y}_2\text{O}_3$ NTs, room-temperature PL measurements were performed with the 488 nm Ar^+ laser operated at 0.5 W. The InGaAs detector was cooled by liquid nitrogen. To prepare the PL samples, powders of $\text{Er}^{3+}:\text{Y}_2\text{O}_3$ NTs were added into ethanol, and the mixtures were subsequently sonicated for about 1 min and later air-dried upon deposition onto silicon wafers.

Results and Discussion

Structural Characterization of $\text{Er}^{3+}:\text{Y}(\text{OH})_3$ NTs. Figure 1 shows representative XRD patterns of the $\text{Er}^{3+}:\text{Y}(\text{OH})_3$ NT powders. These patterns are in agreement with the known hexagonal structures (space group: $P6_3/m$) of $\text{Y}(\text{OH})_3$ and $\text{Er}(\text{OH})_3$ (JCPDS Nos. 24-1422 and 19-0446, respectively).

Typical SEM images of $\text{Er}^{3+}:\text{Y}(\text{OH})_3$ NTs are shown in Figures 2 and S1 and S2 (Supporting Information). These 1-D $\text{Er}^{3+}:\text{Y}(\text{OH})_3$ nanostructures, prepared at temperatures between 100 and 180 °C under hydrothermal conditions, are hollow with a hexagonal cross section. They consist of NTs with a length in the range 2–5 μm , an outer diameter of ~ 100 –400 nm, and an inner diameter of 50–100 nm.

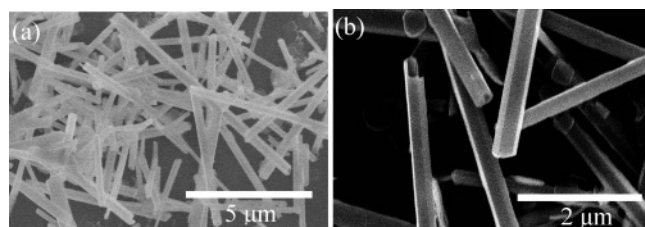


Figure 2. SEM images of $\text{Y}_{0.4}\text{Er}_{0.6}(\text{OH})_3$ NTs synthesized under hydrothermal conditions at 130 °C for 7 h at (a, b) low and high magnifications, respectively.

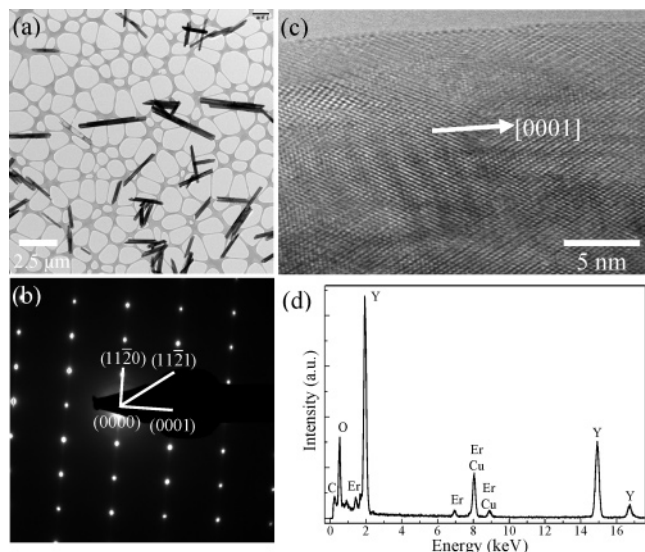


Figure 3. As-prepared $\text{Y}_{0.95}\text{Er}_{0.05}(\text{OH})_3$ NTs synthesized under hydrothermal conditions at 130 °C for 7 h: (a) TEM image; (b) SAED pattern; (c) HRTEM image; (d) EDS data. The Cu and C peaks originate from the TEM grid.

Figure 3a shows a general, low-magnification TEM image of individual $\text{Y}_{0.95}\text{Er}_{0.05}(\text{OH})_3$ NTs. Figure 3b shows a SAED pattern from a single NT, which was indexed to the (0001), (1120), and (1121) diffraction planes, respectively, of the hexagonal structure of $\text{Y}(\text{OH})_3$. Its corresponding HRTEM image is shown in Figure 3c. The identified diffraction planes from the SAED pattern in Figure 3b indicate that the $\text{Y}_{0.95}\text{Er}_{0.05}(\text{OH})_3$ NTs possess a [0001] growth direction. However, the HRTEM image (Figure 3c) could be only indexed to the (400), (040), and (440) planes of cubic Y_2O_3 (Figure S3). It is well-known that hydroxides can dehydrate during experimental microscopy conditions because of the electron bombardment and the high vacuum environment. This possibility is consistent with our observation that the $\text{Er}^{3+}:\text{Y}(\text{OH})_3$ crystal transformed after a few minutes of focused electron beam irradiation and a cubic $\text{Er}^{3+}:\text{Y}_2\text{O}_3$ lattice was formed during the HRTEM imaging. The EDS spectrum (Figure 3d) clearly indicates that this sample is composed of Y, Er, and O elements. Taking into consideration the presence of H in the product, this sample is attributed to $\text{Y}_{0.95}\text{Er}_{0.05}(\text{OH})_3$.

The HAADF image of an as-prepared $\text{Y}_{0.95}\text{Er}_{0.05}(\text{OH})_3$ NT is shown in Figure 4a. The wall of the NT was clearly seen as bright stripes separated by a gray/dark gap. The gray/dark contrast of this gap confirms that these NTs are hollow. HAADF was used due to its greater sensitivity to the atomic number Z (better contrast) than the dark and bright field operation modes. Figure 4b shows the intensity profile of the EDS signal from Y $L\alpha$ radiation (area under the spectrum in the energy range from 1750 to 2300 eV in Figure 3d) along the white line in Figure 4a (perpendicular to the axis of the NT). The signal increased

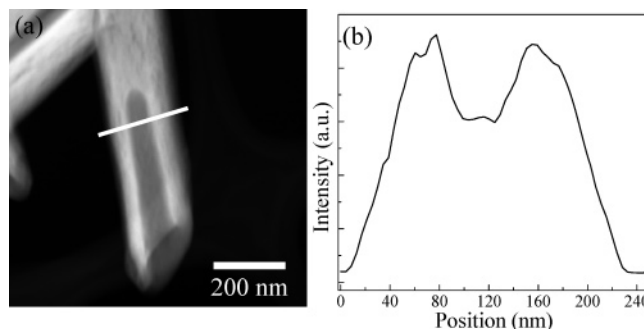


Figure 4. As-prepared $\text{Y}_{0.95}\text{Er}_{0.05}(\text{OH})_3$ NTs synthesized under hydrothermal conditions at 130 °C for 7 h: (a) medium-magnification HAADF image; (b) Y profile across the line in (a).

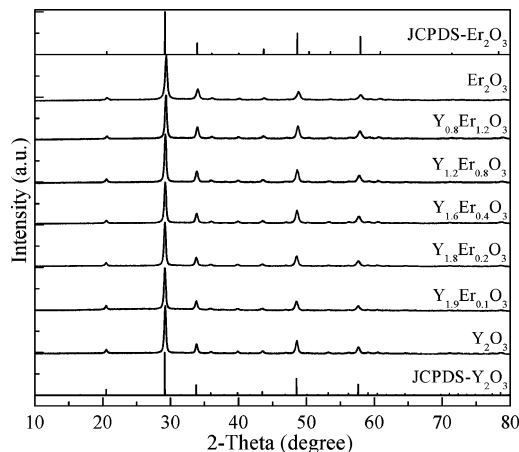


Figure 5. Powder XRD patterns (Cu $K\alpha$) of $\text{Er}^{3+}:\text{Y}_2\text{O}_3$ NTs with various doping levels after annealing the as-synthesized $\text{Er}^{3+}:\text{Y}(\text{OH})_3$ NTs at 500 °C for 3 h.

when the electron beam irradiated the tube walls and decreased, but not to zero, when the electron beam was directed toward the tube axis, resulting in two signal maxima. This profile verifies that the NTs are hollow cylinders.

Structural Characterization of $\text{Er}^{3+}:\text{Y}_2\text{O}_3$ NTs. Powder XRD was used to determine the crystalline phase and purity of the $\text{Er}^{3+}:\text{Y}_2\text{O}_3$ NTs, as shown in Figure 5, in comparison with powder references of Y_2O_3 and Er_2O_3 . These patterns are in agreement with the cubic bixbyite structures (space group: $Ia3$) of Y_2O_3 and Er_2O_3 (JCPDS Nos. 41-1105 and 01-0827, respectively). Synchrotron XRD was used to determine the homogeneous incorporation of the Er^{3+} ions as substituents for the Y^{3+} ions inside the Y_2O_3 host matrix. In Figure 6, the lattice constants of a set of $\text{Er}^{3+}:\text{Y}_2\text{O}_3$, i.e. $(\text{Y}_x\text{Er}_{1-x})_2\text{O}_3$, NT samples were plotted as a function of x , the initial molar fractions of Y^{3+} used in the aqueous solutions for hydrothermal synthesis of $\text{Er}^{3+}:\text{Y}(\text{OH})_3$ NTs. The lattice constant is determined by calculating the cubic cell parameters from the diffraction data of each $\text{Er}^{3+}:\text{Y}_2\text{O}_3$ NT sample. As expected by Vegard's law, the evolution of the lattice constants of the unit cell is linear with x . This clearly demonstrates that the incorporation of Er^{3+} in the Y_2O_3 matrix is quantitative for the $\text{Er}^{3+}:\text{Y}_2\text{O}_3$ NTs and shows that the $\text{Er}^{3+}:\text{Y}_2\text{O}_3$ NT powder samples are single-phase solid solutions. This result is not surprising considering the similar chemical reactivities of Er^{3+} and Y^{3+} ions. The size of the crystalline domains, as obtained from the width of the diffraction peaks using the Scherrer's formula, is about 40 nm.

Figure 7a–f shows typical SEM images of $\text{Er}^{3+}:\text{Y}_2\text{O}_3$ NTs with different doping levels. Figure 8a shows a representative TEM image from the as-synthesized $\text{Y}_{1.9}\text{Er}_{0.1}\text{O}_3$ NTs, corresponding to Figure 7b, and Figure S4. From these images, the

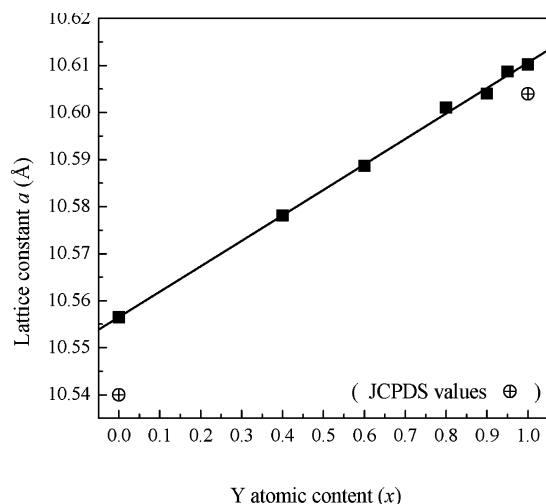


Figure 6. Lattice constants determined by synchrotron XRD for Er^{3+} : Y_2O_3 NTs with various doping levels after annealing the as-synthesized Er^{3+} : $\text{Y}(\text{OH})_3$ NTs at 500 °C for 3 h.

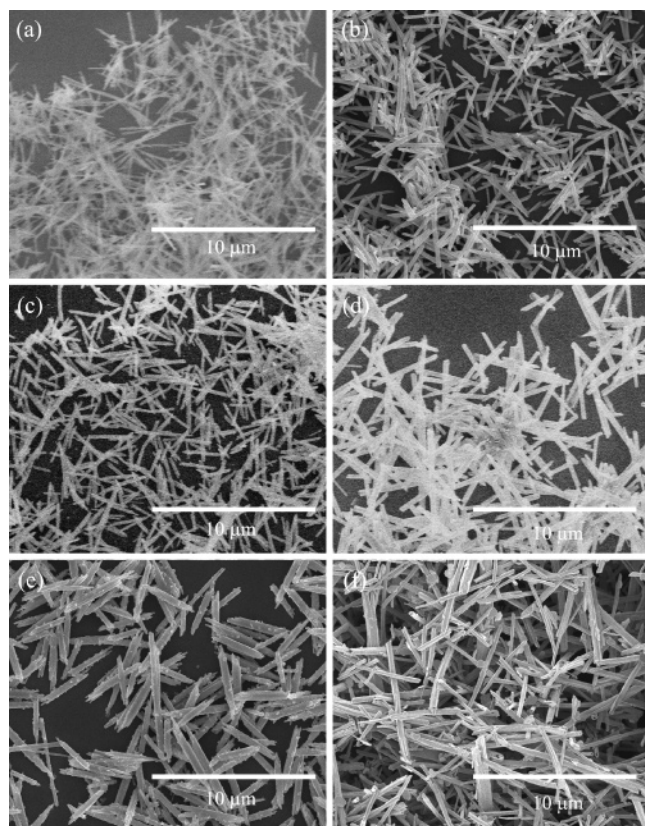


Figure 7. SEM images of Er^{3+} : Y_2O_3 NTs with various doping levels after annealing the as-synthesized Er^{3+} : $\text{Y}(\text{OH})_3$ NTs at 500 °C for 3 h: (a) Y_2O_3 ; (b) $\text{Y}_{1.9}\text{Er}_{0.1}\text{O}_3$; (c) $\text{Y}_{1.8}\text{Er}_{0.2}\text{O}_3$; (d) $\text{Y}_{1.6}\text{Er}_{0.4}\text{O}_3$; (e) $\text{Y}_{1.2}\text{Er}_{0.8}\text{O}_3$; (f) $\text{Y}_{0.8}\text{Er}_{1.2}\text{O}_3$.

as-prepared NTs were measured to be a few micrometers long and ~ 100 – 400 nm in diameter. Though these NTs tended to aggregate, as can be seen from the SEM images (Figure 7), sonication could readily resolve this issue, as shown in the corresponding TEM images (Figures 8a and S4). From these data, it is clear that the Er^{3+} : $\text{Y}(\text{OH})_3$ NTs remain hollow after the dehydration process. The basic 1-D topological morphology of the initial Er^{3+} : $\text{Y}(\text{OH})_3$ NTs (Figures 2 and 3) was found to be preserved after a moderate high-temperature annealing process to form Er^{3+} : Y_2O_3 NTs (Figures 7 and 8). This observation

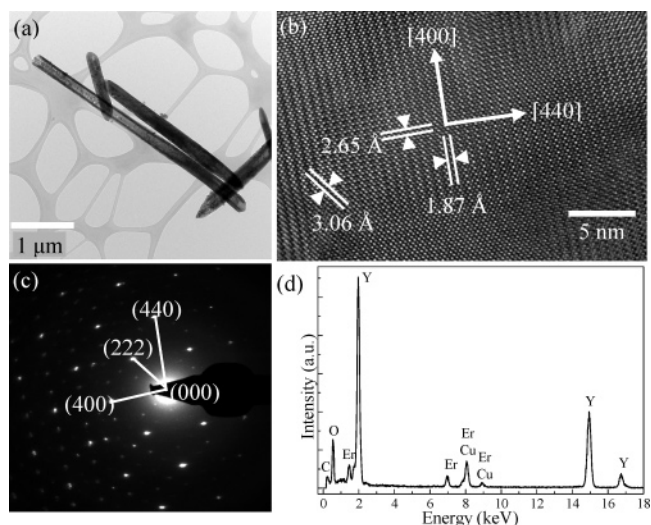


Figure 8. As-prepared $\text{Y}_{1.9}\text{Er}_{0.1}\text{O}_3$ NTs after annealing the as-synthesized 5% doped Er^{3+} : $\text{Y}(\text{OH})_3$ NTs at 500 °C for 3 h: (a) TEM image; (b) HRTEM image; (c) SAED pattern; (d) EDS data. The Cu and C peaks originate from the TEM grid.

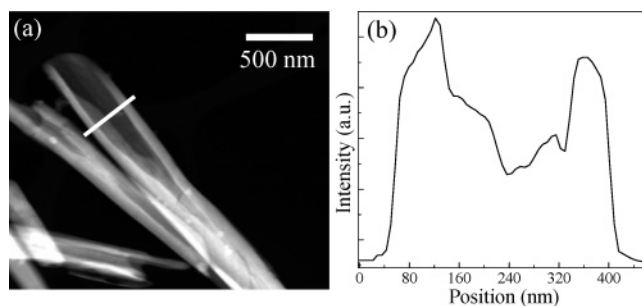


Figure 9. As-prepared $\text{Y}_{1.9}\text{Er}_{0.1}\text{O}_3$ NTs after annealing the as-synthesized 5% doped Er^{3+} : $\text{Y}(\text{OH})_3$ NTs at 500 °C for 3 h: (a) medium-magnification HAADF image; (b) Y profile across the line in (a).

suggests that the initial Er^{3+} : $\text{Y}(\text{OH})_3$ structural motifs were unaffected by the subsequent chemical transformations.

The HRTEM image shown in Figure 8b revealed interlayer spacings measured at 1.87, 2.65, and 3.06 Å, which could be indexed to d_{400} , d_{440} , and d_{222} of cubic Y_2O_3 . Figure 8c shows an SAED pattern, which can be indexed to the (400), (440), and (222) diffraction planes, respectively, of cubic Y_2O_3 , consistent with the HRTEM analysis. The EDS spectrum (Figure 8d) clearly indicates that the $\text{Y}_{1.9}\text{Er}_{0.1}\text{O}_3$ NTs are composed solely of Y, Er, and O elements.

Figures 9a and S4 show HAADF images of as-prepared $\text{Y}_{1.9}\text{Er}_{0.1}\text{O}_3$ NTs. The walls of the Er^{3+} : Y_2O_3 NTs could still be clearly seen as bright stripes separated by a gray/dark gap. The gray/dark contrast of this gap confirms that these Er^{3+} : Y_2O_3 NTs are hollow. The intensity profile (Figure 9b) of the Y $L\alpha$ EDS signal along the white line in Figure 9a (perpendicular to the axis of the NT) verifies that the Er^{3+} : Y_2O_3 NTs are hollow cylinders (Figure 9b), as characterized by two signal maxima.

Plausible Growth Mechanism of Er^{3+} : $\text{Y}(\text{OH})_3$ NTs. To determine the growth mechanism of Er^{3+} : $\text{Y}(\text{OH})_3$ NTs, the effects of chemical composition of the precursor solution on the size, morphology, and crystal structure of the as-synthesized Er^{3+} : $\text{Y}(\text{OH})_3$ nanostructures were investigated. At a NaOH concentration below 0.15 M, only platelike Er-doped yttrium hydroxide nitrate⁵⁵ was obtained (Figure S5a). When the NaOH concentration increased above 1 M, Er^{3+} : $\text{Y}(\text{OH})_3$ NTs with a pure hexagonal crystal phase and uniform 1-D morphology were synthesized (Figure S5b,c). The concentration of $\text{Y}(\text{NO}_3)_3$ and

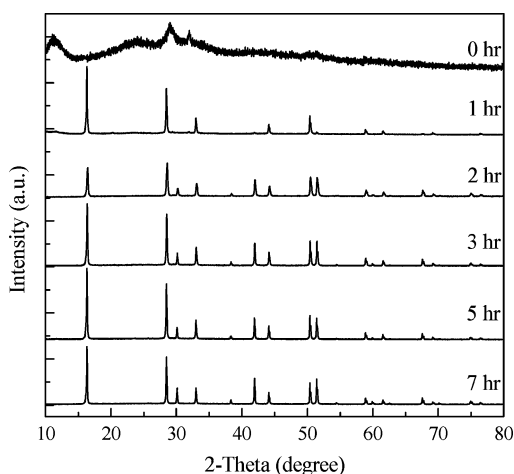


Figure 10. XRD patterns of $\text{Y}_{0.9}\text{Er}_{0.1}(\text{OH})_3$ nanostructures synthesized under hydrothermal conditions at 130 °C with different reaction times.

the time span for adding the NaOH solution, t_{NaOH} , were also shown to control the growth of $\text{Er}^{3+}:\text{Y}(\text{OH})_3$ nanostructure. At a high $\text{Y}(\text{NO}_3)_3$ concentration of 1.5 mmol/18 mL, NTs were synthesized only when NaOH was added slowly over an extended t_{NaOH} (i.e., around 10 min by continuously adding 2 M NaOH solution dropwise, Figures S6a and S7a,b), but no NTs (only platelike structure) were generated at a short t_{NaOH} (as short as 1 s by pouring the entire NaOH solution into the nitrate solution, Figures S6b and S7c,d). At a low $\text{Y}(\text{NO}_3)_3$ concentration (in this case, 0.15 mmol/18 mL), however, 1-D structures were formed even with a t_{NaOH} of 1 s (Figures S6c and S7e,f). This phenomenon is probably similar to what was observed in the synthesis of calcium carbonate where the crystallinity, crystalline polymorph, size, and morphology of products are strongly dependent on the type and the time span of adding synthetic additives and external force.^{56–60} On the other hand, even though nearly identical NTs have been synthesized at temperatures between 100 and 180 °C, the growth process is believed to be temperature-dependent, since some small particles could still be found after hydrothermal treatment at 100 °C (Figure S2).

The effect of the ionic strength of the precursor solution was assessed by adding NaNO_3 into the precursor solution to a concentration as high as 1 M (Figure S8). From the SEM images and XRD patterns, no significant differences were observed between the samples prepared with and without NaNO_3 , except that some nanoparticles were present on the surface of the NTs when NaNO_3 was added. This indicates that the variation of $[\text{NO}_3^-]$ and $[\text{Na}^+]$ due to the concentration change of $\text{Y}(\text{NO}_3)_3$ and NaOH probably does not have a significant effect on the phase and morphology of final products but changes the reaction kinetics. Furthermore, the time-dependent morphological evolution of these $\text{Er}^{3+}:\text{Y}(\text{OH})_3$ NTs in the presence of NaOH was analyzed ex-situ by XRD (Figure 10), SEM (Figure 11), and TEM (Figure 12). Before the hydrothermal process, the gellike precipitate was ill-crystallized and sheetlike, as confirmed by the few broad peaks in the XRD pattern (Figure 10) and the SEM (Figure 11a) and TEM (Figure 12a) images. After 1 h of hydrothermal treatment, the crystallinity improved (Figure 10) and some 1-D nanostructures appeared among the sheetlike material (Figures 11b and 12b). Another 1 h later, some nanoparticles in addition to the sheetlike material and 1-D nanostructures were observed (Figures 11c and 12c). After 3 h of hydrothermal processing, the amount of sheetlike material decreased to only a small portion of the sample (Figures 11d and 12d). Only nanoparticles and 1-D nanostructures were

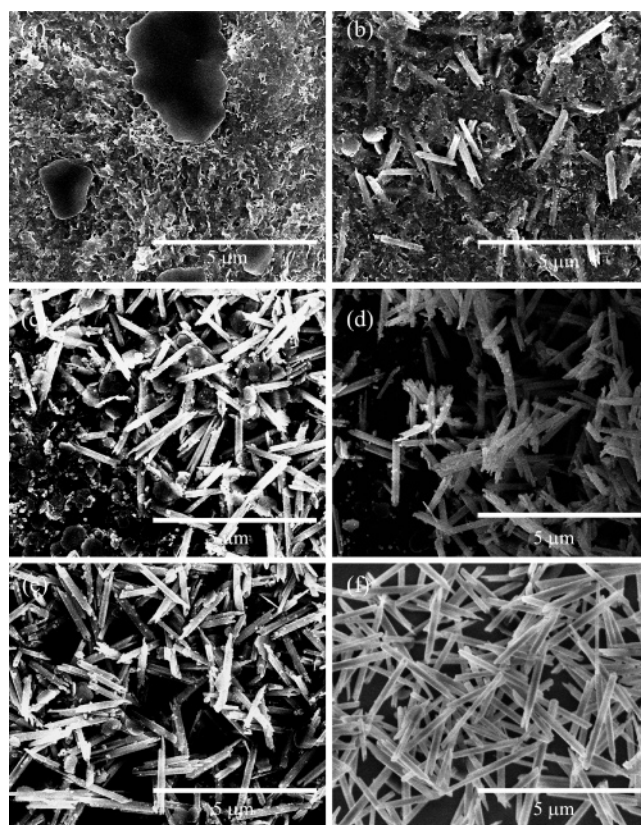


Figure 11. SEM images of $\text{Y}_{0.9}\text{Er}_{0.1}(\text{OH})_3$ nanostructures synthesized under hydrothermal conditions at 130 °C with different reaction times: (a) 0 h; (b) 1 h; (c) 2 h; (d) 3 h; (e) 5 h; (f) 7 h.

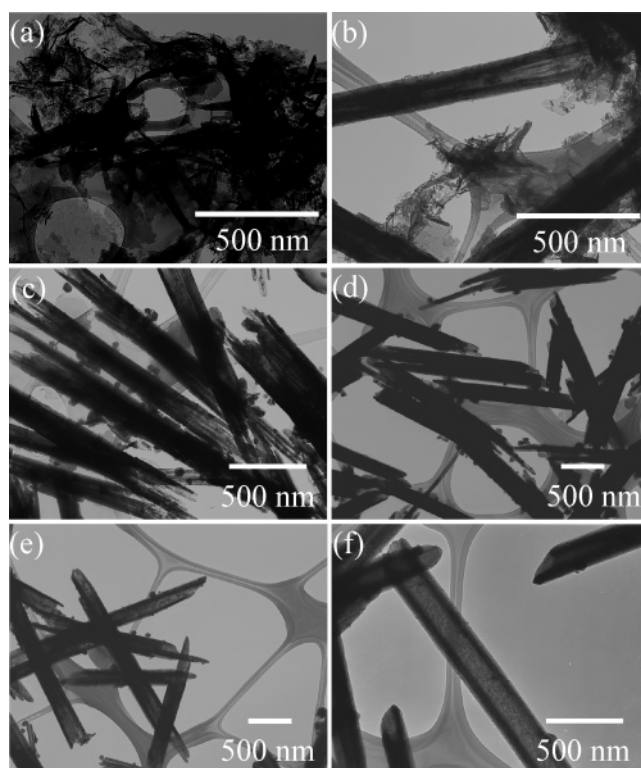


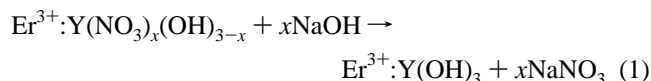
Figure 12. TEM images of $\text{Y}_{0.9}\text{Er}_{0.1}(\text{OH})_3$ nanostructures synthesized under hydrothermal conditions at 130 °C with different reaction times: (a) 0 h; (b) 1 h; (c) 2 h; (d) 3 h; (e) 5 h; (f) 7 h.

present in the sample after 5 h of hydrothermal process. These 1-D nanostructures were hollow at the two ends with groovelike morphology (Figures 11e and 12e).⁶¹ An additional 2 h of

hydrothermal treatment yielded only pure NTs (Figures 11f and 12f). Hence, like other chemical routes to nanostructured materials, the present process also proceeded through nucleation and growth steps, likely involving the nanoparticles seeds.⁶²

The intrinsic crystallographic structures of hexagonal Y(OH)₃ and Er(OH)₃ determine their anisotropic growth under the current hydrothermal conditions, a common phenomenon for many solid materials.²⁹ Specifically, in the hexagonal crystallographic structures of Y(OH)₃ and Er(OH)₃, *P*6₃/*m*, the cations, Y³⁺ and Er³⁺, are located at 2*c* (1/3, 2/3, 1/4) sites (Figure S9). They form infinite linear chains along the *c*-axis, in which the distance between each of two neighboring metal atoms are the same with the unit cell parameter *c* (Figure S9c). Each chain is surrounded by three other chains, which are displaced by *c*/2 with respect to the central one (Figure S9b). As a result, hexagonal channels are formed where the OH[−] groups are inserted. Therefore, the atomic interactions along the *a*- and *b*-directions are much weaker than that along the *c*-axis, and the hexagonal Y(OH)₃ and Er(OH)₃ show a strong preferential growth along the *c*-axis, which corresponds well to the [0001] lattice direction, in agreement with SAED pattern and HRTEM observation (Figure 3b,c).³⁹

During the NT growth process, as shown in Figures 11b–e and 12b–e, the 1-D nanostructures were neither solid nanowires nor NTs with flat ends. They were groove-like nanostructures with nonuniform ends. Moreover, the observed effects of pH, concentration, and ionic strength of the precursor solution and the time span of adding the alkaline solution imply that their growth is a kinetics-driven process. In the alkaline solution, the unstable yttrium or erbium-doped yttrium hydroxide nitrate was gradually dissolved under the hydrothermal condition.^{55,63} The original nitrate ligands were substituted by stronger OH[−] ligands.⁴¹ The chemical reaction could be expressed as



When the concentration of NaOH solution is lower than 1 M, this process does not take place effectively (Figure S5). An adequate supply of OH[−] ions shifts this reaction to the right, following Le Chatelier's principle, and to facilitate the growth of Er³⁺:Y(OH)₃ NTs along the *c*-axis. The addition of NaNO₃ shifts the reaction to the left and slows down the formation process of Er³⁺:Y(OH)₃ NTs. For the first time, the ionic strength of the precursor solution is shown to affect the reaction kinetics for this system under hydrothermal conditions (Figure S8).

On the basis of all the information, we believe that the nucleation of Er³⁺:Y(OH)₃ occurs and the nuclei form nanoparticles under the hydrothermal condition. The nanoparticles continue to grow into 1-D structure with a hexagonal cross section due to its anisotropic hexagonal structure, similar to that of ZnO.²⁹ During this process, the unstable hydroxynitrate continuously dissolves, and continuous supplies of Y³⁺/Er³⁺ and OH[−] ions to the rough nanoparticulate seed surfaces (Figures 11c and 12c) would preferentially occur at the circumferential edges of each regular-shape seed because these sites have relatively higher free energies than other surface sites.^{41,61,64} The continuous nucleation of Er³⁺:Y(OH)₃ on the edges of the seeds could diffuse either circumferentially or axially, which induces the Er³⁺:Y(OH)₃ crystal growth along the circumferential and axial directions of the tubes, respectively. The diffusion rate of the latter process dictates whether the final products are NTs or nanowires. If it were a slow diffusion process, nanowires

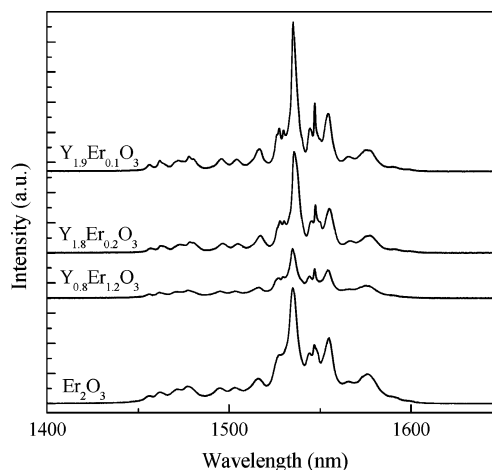


Figure 13. Room-temperature PL spectra of Er³⁺:Y₂O₃ NTs with various doping levels after annealing the as-synthesized Er³⁺:Y(OH)₃ NTs at 500 °C for 3 h (offset for clarification).

would form; on the contrary, when the kinetic condition supported its rapid diffusion, tubes would form with no mass transportation to the inner region. This is because mass transportation to the growing regions would lead to undersaturation in the central part of the growing faces of each seeds as the crystals grow and that “two NTs” could grow on each seed at almost the same rate with opposite direction until no more Y³⁺/Er³⁺ ions are available for the continuous growth. As a result, the concentration of Er³⁺:Y(OH)₃ on the diffusion layer played a crucial role in determining the shape evolution and the final morphology of the Er³⁺:Y(OH)₃. A high concentration of Er³⁺:Y(OH)₃ on the diffusion layer depletes the central growth and gives rise to Er³⁺:Y(OH)₃ NT growth on the nanoparticle seeds, as what have been reported in the growth of Te and *t*-Se NTs.⁶⁴ The decomposition and crystallization of the unstable hydroxide nitrate complex on the surface of the nanoparticle seeds could satisfy this requirement. In other words, the sheetlike hydroxide nitrate complex acted as a local concentration promoter reagent, because such a local concentration on the diffusion layer was much higher than that in the bulk solution. As such, the possible reason for the Er³⁺:Y(OH)₃ NT formation is that the low dissolution rate of Y³⁺/Er³⁺ from the unstable hydroxide nitrate in alkaline solution provided insufficient Y³⁺/Er³⁺ ions for the growth of solid wirelike crystals, and the formation of these hydroxide NTs is a kinetically driven reaction with a diffusion-controlled growth process. In all, both the intrinsic structure and favorable kinetic condition result in the formation of hollow Er³⁺:Y(OH)₃ NTs. A similar growth mechanism has been accounted for the formation of Te and *t*-Se NTs, and our experimental results yield more direct proofs related to the kinetics-controlled reaction mechanisms.^{41,61,64}

Optical Properties of Er³⁺:Y₂O₃ NTs. PL studies of the Er³⁺:Y₂O₃ NTs in the range of 800–1650 nm at room temperature were performed using the 488 nm line of an argon laser as the excitation source. The room-temperature PL spectra characteristic of the ⁴I_{13/2} → ⁴I_{15/2} transition of Er³⁺ ions was clearly observed for all Er³⁺:Y₂O₃ NT samples, at a pump power of 0.5 W (~16 W/cm²) with a 10 s exposure time, as shown in Figures 13 and S10. The maximum intensity occurred at a wavelength of ~1535 nm with a full width at half-maximum of ~4 nm. In literature, the PL spectra for Er-doped SiO₂ thin film samples usually only showed one main peak with a small side shoulder, even at cryogenic temperatures of 77 K or when embedded with Si nanocrystals.^{65,66} On the contrary, the PL

spectra from our $\text{Er}^{3+}:\text{Y}_2\text{O}_3$ NT samples exhibited well-resolved Stark features which corresponded well to the theoretically predicted spectroscopic transitions from the $^4\text{I}_{13/2} \rightarrow ^4\text{I}_{15/2}$ energy manifolds. Near-IR emissions were also observed between 840 and 870 nm corresponding to the $^4\text{S}_{3/2} \rightarrow ^4\text{I}_{13/2}$ transition and between 950 and 1020 nm corresponding to the $^4\text{I}_{11/2} \rightarrow ^4\text{I}_{15/2}$ transition. Specifically, all these optical emissions were assigned to the electronic transitions of Er^{3+} ions in the C_2 sites, as those of Er^{3+} ions in the C_{3i} sites are forbidden due to the inversion symmetry. The remarkably sharp and well-resolved PL spectra around the wavelength of ~ 1535 nm indicate that Er^{3+} ions incorporated in Y_2O_3 NTs by the hydrothermal synthesis followed by the dehydration process occupied well-defined locations in the Y_2O_3 lattice, namely, those of Y^{3+} ions, as confirmed by our EXAFS and XRD analyses.⁶⁷ In general, homogeneous spectral broadening would be observed if an irregular distribution of Er^{3+} in different crystallographic sites (i.e., interstitial sites) happens, which would randomize the Stark splitting. This also indicates that the hydrothermal synthesis followed by the dehydration process for $\text{Er}^{3+}:\text{Y}_2\text{O}_3$ NTs was able to retain the optically active trivalent state of erbium from its precursor state, confirmed by our XANES analysis.⁶⁷ Furthermore, the effective fluorescence line width, $\Delta\lambda_{\text{eff}}$, which is defined as the ratio of integrated fluorescence intensity to peak fluorescence intensity of the fluorescence band at around 1535 nm, is about 30 nm and smaller than that of Er^{3+} -doped ZBLAN glass (about 80 nm),⁶⁸ which is widely used as the media of EDFA and takes an important part in the wavelength-division-multiplexing network system for optical communication. The narrow effective fluorescence line width and the well-resolved emission around the wavelength of 1535 nm indicate that the as-prepared $\text{Er}^{3+}:\text{Y}_2\text{O}_3$ NTs are promising media of optical amplifiers and waveguides used in optical communication.

Conclusion

Erbium incorporation with various concentrations in Y_2O_3 nanotubes was demonstrated using a simple and efficient combination of a hydrothermal process and a dehydration reaction. Extensive characterization of these NT samples was performed using SEM, TEM, HRTEM, EDS, SAED, HAADF, and XRD. A possible growth mechanism of $\text{Er}^{3+}:\text{Y}(\text{OH})_3$ NTs was proposed to elucidate their formation, on the basis of detailed experimental investigations under hydrothermal conditions. The $\text{Er}^{3+}:\text{Y}_2\text{O}_3$ NTs, prepared after annealing the as-synthesized $\text{Er}^{3+}:\text{Y}(\text{OH})_3$ NTs at 500 °C for 3 h, range from 100 to 400 nm in outer diameter and 2 to 5 μm in length and possess a controlled composition in the $(\text{Y}_x\text{Er}_{1-x})_2\text{O}_3$ ($0 \leq x \leq 1$) solid solution. They are highly luminescent at around 1535 nm with remarkably sharp and well-resolved PL spectra. This indicates the present synthetic procedure for $\text{Er}^{3+}:\text{Y}_2\text{O}_3$ NTs was able to retain the optically active trivalent state of erbium from its precursor state, i.e., $\text{Er}(\text{NO}_3)_3$. Moreover, in comparison with organic dyes and semiconductor quantum dots, the PL spectral line width of $\text{Er}^{3+}:\text{Y}_2\text{O}_3$ NTs was narrower. These NTs are probably more stable against photobleaching. These materials are promising for small and compact planar optical amplifiers, lasers, and active waveguides in telecommunication applications. However, further studies are required to improve the size controllability and to study the possible assembling strategies to organize them onto both flexible and rigid substrates for proposed optical and electronic applications.

Acknowledgment. We acknowledge the financial and program support from National Science Foundation (Grant

CTS0522534), the Office of Naval Research (a Young Investigator Award), and the Microelectronics Advanced Research Corp. (MARCO) and its Center on Functional Engineered Nano Architectonics (FENA). The Center for Integrated Nanotechnologies, a U.S. Department of Energy, Office of Basic Energy Sciences, user facility, is supported by Laboratory Directed Research and Development (LDRD), Sandia National Laboratories. Sandia is a multiprogram laboratory operated by Sandia Corp., a Lockheed Martin Co., for the U.S. Department of Energy's National Nuclear Security Administration under Contract DE-AC04-94AL85000. We thank Dr. Michael Toney for his assistance with the synchrotron XRD experiments.

Supporting Information Available: XRD, SEM, HAADF, and PL data. This material is available free of charge via the Internet at <http://pubs.acs.org>.

References and Notes

- (1) Blasse, G.; Grabmeier, B. C. *Luminescent Materials*; Springer-Verlag: Berlin, 1994.
- (2) Justel, T.; Nikol, H.; Ronda, C. *Angew. Chem., Int. Ed.* **1998**, *37*, 3084.
- (3) Ozawa, L.; Itoh, M. *Chem. Rev.* **2003**, *103*, 3835.
- (4) Auzel, F. *Chem. Rev.* **2004**, *104*, 139.
- (5) Kenyon, A. J. *Prog. Quantum Electron.* **2002**, *26*, 225.
- (6) Steckl, A. J.; Zavada, J. M. *MRS Bull.* **1999**, *24* (9), 16 and references therein.
- (7) Nakanishi, Y.; Kimura, K.; Kominami, H.; Nakajima, H.; Hatanaka, Y.; Shimaoka, G. *Appl. Surf. Sci.* **2003**, *212–213*, 815.
- (8) Zhang, W.; Xu, M.; Zhang, W.; Yin, M.; Qi, Z.; Xia, S.; Claudine, G. *Chem. Phys. Lett.* **2003**, *376*, 318.
- (9) Ballato, J.; Lewis, J. S., III; Holloway, P. *MRS Bull.* **1999**, *24* (9), 51.
- (10) Vetrone, F.; Boyer, J.-C.; Capobianco, J. A. In *Encyclopedia of Nanoscience and Nanotechnology*; Nalwa, H. S., Ed.; American Scientific Publishers: Stevenson Ranch, CA, 2004; Vol. 10, p 725.
- (11) Dejneka, M.; Samson, B. *MRS Bull.* **1999**, *24* (9), 39.
- (12) Polman, A. *J. Appl. Phys.* **1997**, *82*, 1.
- (13) Van, T. T.; Hoang, J.; Ostroumov, R.; Wang, K. L.; Bargar, J. R.; Lu, J.; Blom, H.-O.; Chang, J. P. *J. Appl. Phys.* **2006**, *100*, 073512.
- (14) Zhang, J.; Wang, S.; Rong, T.; Chen, L. *J. Am. Ceram. Soc.* **2004**, *87*, 1072.
- (15) Dikovska, A. O. G.; Atanasov, P. A.; Castro, M. J. d.; Perea, A.; Gonzalo, J.; Afonso, C. N.; Lopez, J. G. *Thin Solid Films* **2006**, *500*, 336.
- (16) Flores-Gonzalez, M. A.; Lebbou, K.; Bazzi, R.; Louis, C.; Perriat, P.; Tillement, O. *J. Cryst. Growth* **2005**, *277*, 502.
- (17) Si, R.; Zhang, Y.-W.; Zhou, H.-P.; Sun, L.-D.; Yan, C.-H. *Chem. Mater.* **2007**, *19*, 18.
- (18) Van, T. T.; Chang, J. P. *Appl. Phys. Lett.* **2005**, *87*, 011907.
- (19) Masuda, Y.; Yamagishi, M.; Koumoto, K. *Chem. Mater.* **2007**, *19*, 1002.
- (20) Vetrone, F.; Boyer, J.-C.; Capobianco, J. A.; Speghini, A.; Bettinelli, M. *Chem. Mater.* **2003**, *15*, 2737.
- (21) Eilers, H. *Mater. Lett.* **2006**, *60*, 214.
- (22) Capobianco, J. A.; Vetrone, F.; Boyer, J. C.; Speghini, A.; Bettinelli, M. *J. Phys. Chem. B* **2002**, *106*, 1181.
- (23) Qi, Z.; Shi, C.; Zhang, W.; Zhang, W.; Hu, T. *Appl. Phys. Lett.* **2002**, *81*, 2857.
- (24) Soo, Y. L.; Huang, S. W.; Kao, Y. H.; Chhabra, V.; Kulkarni, B.; Veliadis, J. V. D.; Bhargava, R. N. *Appl. Phys. Lett.* **1999**, *75*, 2464.
- (25) Allieri, B.; Depero, L. E.; Marino, A.; Sangaletti, L.; Caporaso, L.; Speghini, A.; Bettinelli, M. *Mater. Chem. Phys.* **2000**, *66*, 164.
- (26) Lee, S.-Y.; Gao, X.; Matsui, H. *J. Am. Chem. Soc.* **2007**, *129*, 2954.
- (27) Sivakumar, S.; Veggel, F. C. J. M. v.; May, P. S. *J. Am. Chem. Soc.* **2007**, *129*, 620.
- (28) Li, Y.; Qian, F.; Xiang, J.; Lieber, C. M. *Mater. Today* **2006**, *9* (10), 18.
- (29) Xia, Y.; Yang, P.; Sun, Y.; Wu, Y.; Mayers, B.; Gates, B.; Yin, Y.; Kim, F.; Yan, H. *Adv. Mater.* **2003**, *15*, 353.
- (30) Liu, G.; Hong, G. *J. Nanosci. Nanotechnol.* **2006**, *6*, 120.
- (31) Wu, G. S.; Lin, Y.; Yuan, X. Y.; Xie, T.; Cheng, B. C.; Zhang, L. *D. Nanotechnology* **2004**, *15*, 568.
- (32) Yang, L.; Tang, Y.; Chen, X.; Li, Y.; Cao, X. *Mater. Chem. Phys.* **2007**, *101*, 195.
- (33) Wang, X.; Sun, X.; Yu, D.; Zou, B.; Li, Y. *Adv. Mater.* **2003**, *15*, 1442.
- (34) De, G.; Qin, W.; Zhang, J.; Zhang, J.; Wang, Y.; Cao, C.; Cui, Y. *J. Lumin.* **2006**, *119–120*, 258.

- (35) Wang, X.; Li, Y. *Chem.—Eur. J.* **2003**, *9*, 5627.
- (36) Bai, X.; Song, H.; Yu, L.; Yang, L.; Liu, Z.; Pan, G.; Lu, S.; Ren, X.; Lei, Y.; Fan, L. *J. Phys. Chem. B* **2005**, *109*, 15236.
- (37) Wu, G.; Zhang, L.; Cheng, B.; Xie, T.; Yuan, X. *J. Am. Chem. Soc.* **2004**, *126*, 5976.
- (38) Tang, B.; Ge, J.; Wu, C.; Zhuo, L.; Niu, J.; Chen, Z.; Shi, Z.; Dong, Y. *Nanotechnology* **2004**, *15*, 1273.
- (39) Fang, Y.-P.; Xu, A.-W.; You, L.-P.; Song, R.-Q.; Yu, J. C.; Zhang, H.-X.; Li, Q.; Liu, H.-Q. *Adv. Funct. Mater.* **2003**, *13*, 955.
- (40) Rajasekharan, V. V.; Buttry, D. A. *Chem. Mater.* **2006**, *18*, 4541.
- (41) Tang, Q.; Liu, Z.; Li, S.; Zhang, S.; Liu, X.; Qian, Y. *J. Cryst. Growth* **2003**, *259*, 208.
- (42) Xu, Z.; Hong, Z.; Zhao, Q.; Peng, L.; Zhang, P. *J. Rare Earths* **2006**, *24*, 111.
- (43) Capobianco, J. A.; Vetrone, F.; D'Alesio, T.; Tessari, G.; Speghini, A.; Bettinelli, M. *Phys. Chem. Chem. Phys.* **2000**, *2*, 3203.
- (44) Pires, A. M.; Serra, O. A.; Heer, S.; Gudel, H. U. *J. Appl. Phys.* **2005**, *98*, 063529.
- (45) Goldys, E. M.; Drozdowicz-Tomsia, K.; Jinjun, S.; Dosev, D.; Kennedy, I. M.; Yatsunenko, S.; Godlewski, M. *J. Am. Chem. Soc.* **2006**, *128*, 14498.
- (46) Anh, T. K.; Minh, L. Q.; Vu, N.; Huong, T. T.; Huong, N. T.; Barthou, C.; Strek, W. *J. Lumin.* **2003**, *102–103*, 391.
- (47) Bhargava, R. N. *J. Cryst. Growth* **2000**, *214–215*, 926.
- (48) Wang, L.; Li, Y. *Chem. Mater.* **2007**, *19*, 727.
- (49) Yan, J.; Estevez, M. C.; Smith, J. E.; Wang, K.; He, X.; Wang, L.; Tan, W. *Nano Today* **2007**, *2* (3), 44.
- (50) Hirai, T.; Orikoshi, T.; Komasaawa, I. *Chem. Mater.* **2002**, *14*, 3576.
- (51) Silver, J.; Martinez-Rubio, M. I.; Ireland, T. G.; Fern, G. R.; Withnall, R. *J. Phys. Chem. B* **2001**, *105*, 948.
- (52) Gordon, W. O.; Tissue, B. M.; Morris, J. R. *J. Phys. Chem. C* **2007**, *111*, 3233.
- (53) Hakuta, Y.; Ura, H.; Hayashi, H.; Arai, K. *Ind. Eng. Chem. Res.* **2005**, *44*, 840.
- (54) Patzke, G. R.; Krumeich, F.; Nesper, R. *Angew. Chem., Int. Ed.* **2002**, *41*, 2446.
- (55) Schildermans, I.; Mullens, J.; Yperman, J.; Franco, D.; Poucke, L. C. V. *Thermochim. Acta* **1994**, *231*, 185.
- (56) Naka, K.; Huang, S.-C.; Chujo, Y. *Langmuir* **2006**, *22*, 7760.
- (57) Aizenberg, J.; Lambert, G.; Weiner, S.; Addadi, L. *J. Am. Chem. Soc.* **2002**, *124*, 32.
- (58) Wang, M.; Zou, H. K.; Shao, L.; Chen, J. F. *Powder Technol.* **2004**, *142*, 166.
- (59) Nikulshina, V.; Galvez, M. E.; Steinfeld, A. *Chem. Eng. J.* **2007**, *129*, 75.
- (60) Zhou, G.-T.; Yu, J. C.; Wang, X.-C.; Zhang, L.-Z. *New J. Chem.* **2004**, *28*, 1027.
- (61) Xi, G.; Xiong, K.; Zhao, Q.; Zhang, R.; Zhang, H.; Qian, Y. *Cryst. Growth Des.* **2006**, *6*, 577.
- (62) Cushing, B. L.; Kolesnichenko, V. L.; O'Connor, C. J. *Chem. Rev.* **2004**, *104*, 3893.
- (63) Fokema, M. D.; Chiu, E.; Ying, J. Y. *Langmuir* **2000**, *16*, 3154.
- (64) Mayers, B.; Xia, Y. *Adv. Mater.* **2002**, *14*, 279.
- (65) Fujii, M.; Yoshida, M.; Kanzawa, Y.; Hayashi, S.; Yamamoto, K. *Appl. Phys. Lett.* **1997**, *71*, 1198.
- (66) Sun, J. M.; Skorupa, W.; Dekorsy, T.; Helm, M.; Nazarov, A. N. *Opt. Mater.* **2005**, *27*, 1050.
- (67) Mao, Y.; Bargar, J.; Toney, M.; Chang, J. P. *J. Appl. Phys.* submitted for publication.
- (68) Wetenkamp, L.; West, G. F.; Tobben, H. *J. Non-Cryst. Solids* **1992**, *140*, 35.